T_{20} measurements for $^1H(\vec{d},\gamma)^3He$ and the P-wave component of the nucleon-nucleon force

G. J. Schmid, R. M. Chasteler, and H. R. Weller
Duke University, Durham, North Carolina 27708
and Triangle Universities Nuclear Laboratory, Durham, North Carolina 27708

D. R. Tilley
North Carolina State University, Raleigh, North Carolina 27695 and Triangle Universities Nuclear Laboratory, Durham, North Carolina 27708

A. C. Fonseca
Centro Fisica Nuclear, Universidade de Lisboa, P-1699 Lisbon, Portugal

D. R. Lehman
Center for Nuclear Studies, Department of Physics, The George Washington University, Washington, D.C. 20052
(Received 23 January 1995)

Measurements of $T_{20}(\theta_{lab}=90°)$ for $^1H(\vec{d},\gamma)^3He$, in the energy range $E_d(lab)=12.7-19.8$ MeV, have been compared with the results of new exact three-body Faddeev calculations using the Paris and Bonn-*A* nucleon-nucleon (*NN*) potentials. This comparison indicates a strong sensitivity of the T_{20} observable to the *p*-wave part of the *NN* force. In particular, we find that the $^3P_1$ component of the *P*-wave interaction is the dominant *P*-wave term affecting the value of $T_{20}(\theta_{lab}=90°)$ at these energies. This contrasts with the results of polarized *N-D* scattering studies where the $^3P_0$ component has been found to dominate.

PACS number(s): 25.40.Lw, 21.30.Fe, 24.70.+s, 25.10.+s

One of the ongoing topics of study in the field of nuclear physics has been the quest to understand three-body reaction dynamics in terms of two-body nucleon-nucleon (*NN*) interactions. The $^1H(\vec{d},\gamma)^3He$ reaction plays an important role in this quest in that it provides a testing ground for the description of polarized, photonuclear observables. Recently, Fonseca and Lehman have provided detailed results of a $^1H(\vec{d},\gamma)^3He$ Faddeev calculation [1] which was performed using exact three-body dynamics in both the initial and final states, and which used the Paris potential [2] for the *NN* interaction. The focus was on the tensor analyzing power (TAP) polarized observables, which have been shown [3] to arise due to the presence of a *D* state in the ground state wave function (the existence of the *D* state being a consequence of the tensor component of the *NN* force). Upon comparison of the theoretical results with the available TAP data from the $^1H(\vec{d},\gamma)^3He$ reaction, it was found that the *P*-wave part of the *NN* force played an especially important role at some energies (see also Ref. [4]). Calculations that neglected the *NN P*-wave component (i.e., that used just the traditional *S* and *D* wave *NN* components) were unable to fit all of the TAP data.

The aim of the current work on the $^1H(\vec{d},\gamma)^3He$ reaction has been to provide experimental data which could be used to verify the relative importance of the *NN P* waves in a previously unexplored energy region. In particular, we have measured the tensor analyzing power $T_{20}(\theta)$ at a laboratory angle of 90° for center-of-target beam energies of $E_d(lab)=19.8$, 17.0, 15.0, and 12.7 MeV. New full three body calculations have also been performed at these energies in order to allow a more precise comparison of theory and experiment. The energy range that we have chosen to study is significant in the sense that it spans a region where the cumulative effect of the *NN P* waves was predicted to vary from ''negligible'' (~20 MeV) to ''very important'' (~10 MeV) [1]. The results of the current work show that the theoretical T_{20} energy dependence matches the experimental data if and only if the *P*-wave part of the *NN* interaction is included in the calculation, thus verifying the importance of the *NN P* waves in the T_{20} observable. Furthermore, we show that the $^3P_1$ component of the *NN P*-wave force is the strongest *NN P*-wave component in the $^1H(\vec{d},\gamma)^3He$ T_{20} calculation. This result is interesting to compare with the results of polarized nucleon-deuteron (*N-D*) elastic scattering experiments, which have also shown sensitivity to the *NN P* waves. The $^3P_0$ component was identified as the dominant part of the *P*-wave interaction in these studies [5,6].

All the $T_{20}(\theta)$ data in the current $^1H(\vec{d},\gamma)^3He$ experiment were acquired at the Triangle Universities Nuclear Laboratory (TUNL). The tensor polarized deuteron beam was provided by the TUNL Atomic Beam Polarized Ion Source [7] which typically provided 70–80 % of the maximum theoretical value for the t_{20} beam moment. After being polarized, the beam was accelerated to the desired energy by a type FN Tandem Van de Graaff accelerator, and was then passed through a 1 mil thick Kapton entrance foil into a target chamber containing pure hydrogen gas. A diagram of the target-detector geometry is shown in Fig. 1, [8] whereby the deuteron beam is incident at the bottom of the figure. The γ-ray spectra from $^1H(\vec{d},\gamma)^3He$ were obtained with an anti-coincidence shielded 25.4 cm×25.4 cm cylindrical NaI(Tl) detector which was surrounded with lithium carbonated paraffin to reduce neutron background. Lead collimators were placed in front of the NaI detector in order to define a H_2 gas target length of 10.8 cm.

 © 1996 The American Physical Society

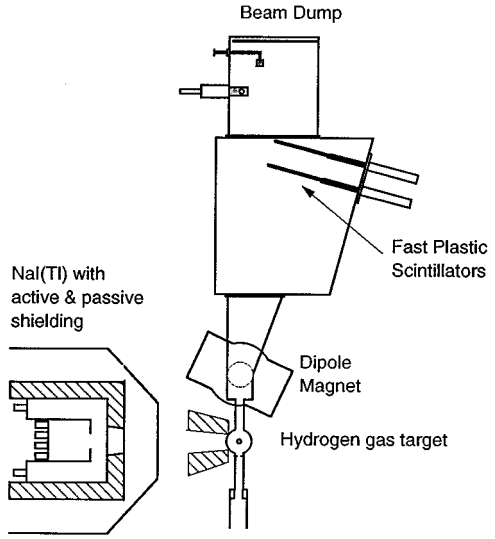

FIG. 1. The experimental setup for the current $^1\mathrm{H}(\vec{d},\gamma)^3\mathrm{He}$ experiment. Shown are the hydrogen gas target, the NaI(Tl) γ-ray detector, the dipole bending magnet, and the ^{3}He recoil box containing the fast plastic scintillators for detecting the ^{3}He recoils.

In order to further reduce the neutron induced background, a ^{3}He recoil coincidence setup was used. In this setup, the ^{3}He recoils from the $^1\mathrm{H}(\vec{d},\gamma)^3\mathrm{He}$ reaction were allowed to pass out of the target chamber by means of a 0.5 mil Kapton exit foil. As shown in Fig. 1, the ^{3}He recoils were then deflected out of the exiting deuteron beam by means of a dipole bending magnet, and were subsequently detected by a fast plastic scintillator which was located approximately 1.8 meters downstream of the target center. While the majority of the exiting deuteron beam was collected in a tantalum lined beam dump further downstream, a small fraction of the deuteron beam halo wound up hitting the scintillator along with the ^{3}He recoils. In order to veto out these unwanted events, a second scintillator was employed. Since the thickness of the first scintillator was set so as to completely stop the ^{3}He recoils but not the deuterons, the errant deuterons passed through the first scintillator (depositing some energy there), and were then incident upon the second scintillator (also depositing some energy there). By monitoring coincidences between the two scintillators, all unwanted events could be vetoed out, and thus a pure ^{3}He recoil spectrum could be obtained.

A time to amplitude converter (TAC) was used to effect the coincidence requirement between the $^1\mathrm{H}(\vec{d},\gamma)^3\mathrm{He}$ γ ray and the recoiling ^{3}He nucleus. By starting the TAC with a γ-ray count in the NaI(Tl) detector, and stopping the TAC with a ^{3}He recoil event in the front plastic scintillator, a spectrum such as the one shown in Fig. 2 is obtained (over the course of one experimental run). By selecting only those γ rays which correspond to γ ray/^{3}He coincidences (the peak enclosed by the dashed lines in Fig. 2), we can obtain clean γ-ray spectra such as the one shown in Fig. 3(a). The $^1\mathrm{H}(\vec{d},\gamma)^3\mathrm{He}$ peak in Fig. 3(a) is clearly visible at 12 MeV, while the discriminator threshold causes the dropoff seen at about 9 MeV. The γ-ray spectrum shown in Fig. 3(a) can be further improved by subtracting out the random TAC coincidences represented by the constant background in Fig. 2. Once this is done, we obtain the final background subtracted

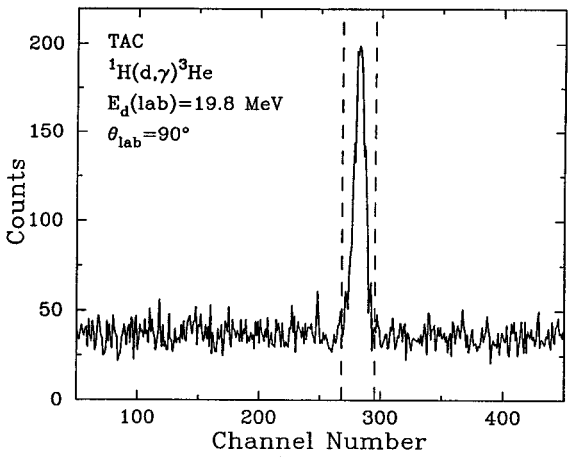

FIG. 2. The TAC spectrum which is created by a start signal from the NaI(Tl) γ-ray detector and a stop signal from the fast plastic scintillator (which detects the ^{3}He recoils). The peak represents true coincidences, while the flat background represents random coincidences.

spectrum shown in Fig. 3(b). In order to obtain a yield from this spectrum, we can sum the peak in the region enclosed by the dashed lines. This region represents an energy spread corresponding to two widths down and one width up from the peak centroid.

The measurement of the tensor analyzing power $T_{20}(\theta)$ was performed by allowing the polarized ion source to fast spin flip between two tensor polarized deuteron spin states at a rate of 10 Hertz. The two spin states reflect, respectively, a 0% and a 66% population of the $m_j=0$ substate. A Wien

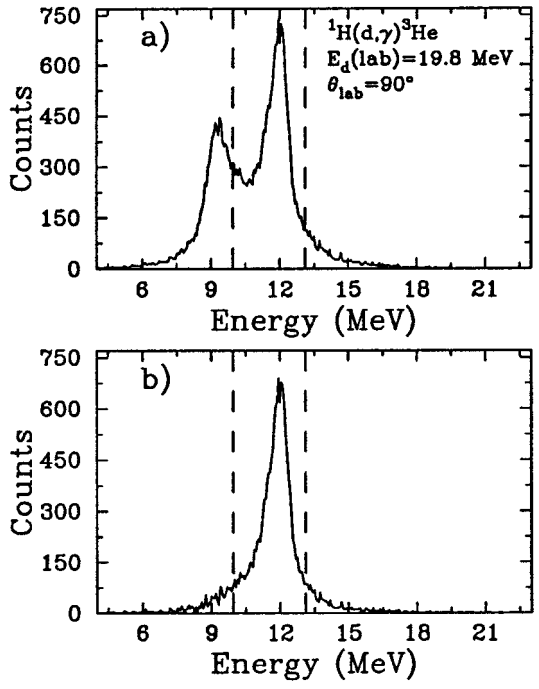

FIG. 3. The TAC-gated energy spectrum for the $^1\mathrm{H}(\vec{d},\gamma)^3\mathrm{He}$ reaction at E_d(lab)=19.8 MeV and θ_{lab}=90° before (a) and after (b) subtracting out the off-TAC peak background. The γ-ray peak of interest is at 12 MeV, while the threshold cutoff is at 9 MeV.

TABLE I. T_{20} data for $^1H(\vec{d},\gamma)^3He$.

E_d (lab)	θ (lab)	$T_{20}(\theta)$	Error
19.8 MeV	90°	−0.054	0.012
19.8 MeV	105°	−0.044	0.012
17.0 MeV	90°	−0.047	0.010
15.0 MeV	90°	−0.038	0.008
12.7 MeV	90°	−0.023	0.006

filter was used to align the spin symmetry axis along the beam axis (β=0). The yield, $Y_1(\theta)$, which results from the $^1H(\vec{d},\gamma)^3He$ reaction initiated by polarized deuterons in spin state 1 (beam moment t_{20}) is related to the unpolarized yield, $Y_0(\theta)$, by [9]

$$Y_1(\theta)=Y_0(\theta)[1+t_{20}T_{20}(\theta)]. \quad (1)$$

And similarly for the polarized yield $Y_2(\theta)$ for spin state 2 (beam moment t'_{20}):

$$Y_2(\theta)=Y_0(\theta)[1+t'_{20}T_{20}(\theta)]. \quad (2)$$

Combining the above two equations in order to eliminate $Y_0(\theta)$, we obtain

$$T_{20}(\theta)=\frac{Y_1(\theta)-Y_2(\theta)}{Y_2(\theta)t_{20}-Y_1(\theta)t'_{20}}. \quad (3)$$

Equation (3) is the expression used to tabulate the $T_{20}(\theta)$ values from the raw experimental yields. The beam moments t_{20} and t'_{20} were measured periodically by tuning the beam down a separate beam line into a $^3He(\vec{d},p)^4He$ polarimeter [10]. Table I shows the final results of our $T_{20}(\theta)$ measurements for the $^1H(\vec{d},\gamma)^3He$ reaction. The error bars include contributions from both counting statistics and beam polarization uncertainties (but the contributions of the latter are negligible). The data that were taken at 19.8 MeV are in excellent agreement with the published results of Vetterli *et al.*[11]. This agreement is shown in Fig. 4, where the *x*'s are the previously acquired data points of Vetterli *et al.* [11] and the open circles are the two currently acquired data points at E_d(lab)=19.8 MeV.

Figure 5 shows, by the open circles, the currently acquired $T_{20}(\theta)$ data at θ_{lab}=90° for all the center-of-target beam energies that we have measured. The point at 19.8 MeV is a weighted average of our point (θ_{lab}=90°) with two of the Vetterli *et al.* points [11] which have corresponding laboratory angles of 86° and 94° (±3). These angles are well within the angular resolution of our $T_{20}(\theta)$ data point at 90° [the angular resolution of our NaI(Tl) detector was about ±10°]. Also shown in Fig. 5 is a previous $T_{20}(\theta)$ data point at θ_{lab}=82° that was published in the reference quoted (Ref. [12]). The value of the $T_{20}(\theta)$ at θ_{lab}=82° is not expected to be appreciably different from the θ_{lab}=90° value (see the measured angular distribution in Fig. 4). The three curves shown in Fig. 5 are the theoretical results of new exact three body calculations for the T_{20} observable at θ_{lab}=90°. The theoretical results at E_d(lab)=10.0 and 19.8 MeV have been previously published [1], but the other points are new. The initial and final state wave functions in these calculations are derived using either the Paris *NN* potential [2] (solid and dashed lines) or the Bonn *A NN* potential [13,14] (dotted line) in the EST expansion [15]. The Coulomb interaction between the two protons has been neglected. The neglect of the Coulomb interaction at these energies (well above the Coulomb barrier) is justified based on experimental evidence [16] showing that $p+D$ and $n+D$ analyzing powers are not significantly different in this regime. The matrix elements are calculated using the Siegert form of the $E1$ operator (in the long wavelength approximation). While the lack of $M1$ transitions is expected to affect $T_{20}(\theta)$ at extreme angles, the effect at more central angles (near 90°) is thought to be negligible [17]. The lack of transitions higher than dipole (i.e.,

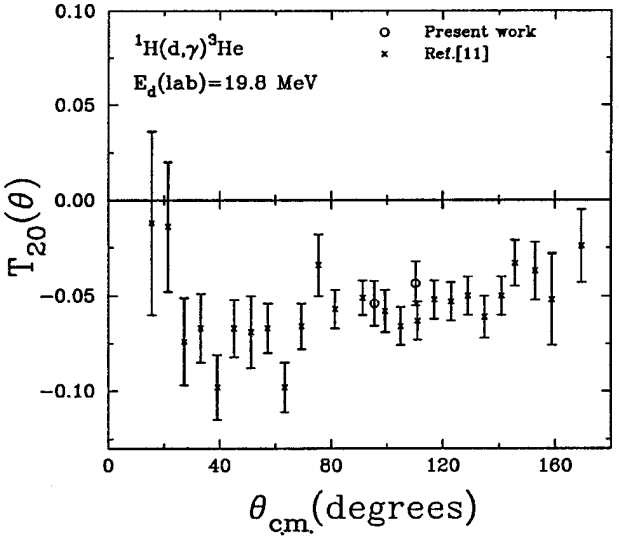

FIG. 4. Current $^1H(\vec{d},\gamma)^3He$ results at E_d(lab)=19.8 MeV, represented by the open data points, are shown along with the previously acquired data of Vetterli *et al.* [11] (*x*'s).

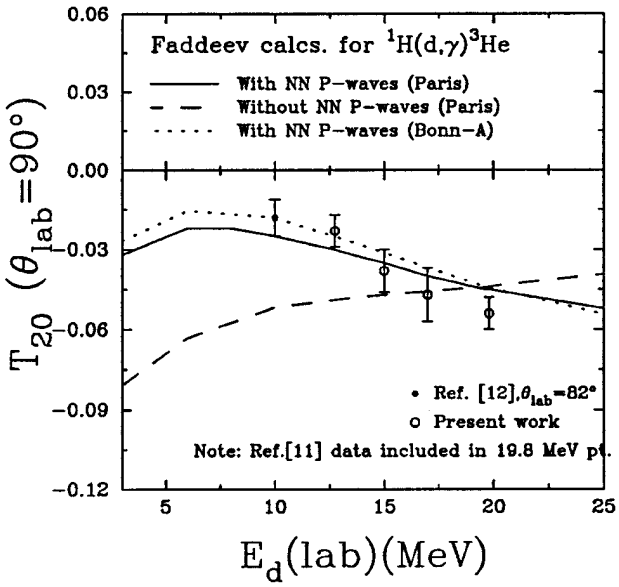

FIG. 5. The $T_{20}(\theta_{lab}$=90°) data that we have acquired in the current $^1H(\vec{d},\gamma)^3He$ experiment (open data points), shown along with a previously published data point at E_d(lab)=10 MeV [12] (solid data point). The solid and dashed lines are current theoretical calculations using the Paris *NN* potential, while the dotted line is a current theoretical calculation using the Bonn *A NN* potential.

TABLE II. Results of Faddeev calculations for $^1\mathrm{H}(\vec{d},\gamma)^3\mathrm{He}$, at $E_{d_{\mathrm{lab}}}=8$ MeV, done to identify the dominant *NN P*-wave piece.

Calculation	T_{20} ($\theta_{\mathrm{lab}}=90°$)	Δ (rel. to calc. No. 3)
1. No *NN P* waves	−0.0563	
2. *NN P* waves in gnd. state only	−0.0559	
3. *NN P* waves in gnd. state & continuum	−0.0455	
4. (---)+$^1P_1$ in int. rescatt. state	−0.0497	−0.0042
5. (---)+$^3P_0$ in int. rescatt. state	−0.0359	0.0097
6. (---)+$^3P_1$ in int. rescatt. state	−0.0302	0.0153
7. (---)+$^3P_2$ in int. rescatt. state	−0.0432	0.0023
8. (---)+$^1P_1$,$^3P_0$,$^2P_1$,$^3P_2$ in int. rescatt. st.	−0.0221	0.0235

*E*2 transitions) is not expected to affect the calculations in this energy regime.

The solid curve in Fig. 5 denotes a calculation (using the Paris *NN* potential) where the *NN* interaction is present in the *S*, *P*, and *D* partial waves. In particular, the following *NN* partial wave components are present in this calculation: $^1S_0$, $^3S_1-^3D_1$, $^1P_1$, $^3P_0$, $^3P_1$, and $^3P_2$. The dashed curve in Fig. 5 represents a similar calculation (with the Paris *NN* potential) which, however, has neglected the *NN P* waves, and thus has only the $^1S_0$ and $^2S_1-^3D_1$ partial waves present in the *NN* interaction. The sensitivity of the $T_{20}(90°)$ observable to the *NN P*-wave interaction is clearly demonstrated by the divergence of the two curves as one moves in energy away from E_d(lab)$\sim$20 MeV. In comparing the two curves with the plotted data, it is immediately clear that the full, *P*-wave inclusive, calculation (solid line) gives much better agreement over the energy range presented. The dotted curve in Fig. 5 represents an exact calculation which includes the same *NN*, *S*, *P*, and *D* partial waves as indicated above, but unlike the previous two sets of calculations (the solid and dashed lines), uses the Bonn-*A NN* potential instead of the Paris *NN* potential. It is apparent that the results obtained using the Bonn-*A NN* potential are equivalent to the results obtained using the Paris *NN* potential as far as our data are concerned.

As alluded to in Ref. [1], the importance of the *NN P* waves in the T_{20} calculation may be understood qualitatively in terms of the following argument. The TAP observables in $^1\mathrm{H}(\vec{d},\gamma)^3\mathrm{He}$, as pointed out before, arise from the presence of a *D* state in the ^{3}He ground state. The presence of the *NN P* waves in the continuum allows extra transitions which can couple the intermediate rescattering state to this ^{3}He *D* state via the *E*1 operator (irrespective of the presence of *NN P* waves in the ground state). This occurs because the *E*1 operator (negative parity) can couple the rescattering term involving a nucleon plus a correlated pair of particles with negative parity (*NN P*-wave motion) with the positive parity states in the ^{3}He *D* state. Thus, because the continuum *NN P* waves allow extra transitions to the ^{3}He *D* state, they should be expected to affect the TAP observables such as T_{20}. The extent of this effect, as predicted by the exact three-body calculation using the Paris and Bonn *A NN* potentials, appears to be verified by the available data.

In order to identify the role and sensitivity of the various *NN P*-wave components, new three-body calculations have been performed at E_d(lab)=8.0, 19.8, and 29.2 MeV. The results of these calculations, for T_{20} at $\theta_{\mathrm{lab}}=90°$, are summarized in Tables II–IV. The first calculation presented in the tables includes the *NN* interaction only in the $^1S_0$ and $^3S_1-^3D_1$ partial waves (i.e., the *NN P* waves are neglected). The next calculation includes the *NN P* waves in the ground state only. The third calculation includes the *NN P* waves in the ground and continuum states, but neglects their presence in the intermediate rescattering state. In the next four calculations, each one of the four possible *NN P*-wave components in the intermediate rescattering state is separately turned on in order to gauge its relative strength. By this approach, the $^1S_0$ and $^3S_1-^3D_1$ half-shell rescattering amplitudes are always the same and remain unaffected by truncat-

TABLE III. Results of Faddeev calculations for $^1\mathrm{H}(\vec{d},\gamma)^3\mathrm{He}$, at $E_{d_{\mathrm{lab}}}=19.8$ MeV, done to identify the dominant *NN P*-wave piece.

Calculation	T_{20} ($\theta_{\mathrm{lab}}=90°$)	Δ (rel. to calc. No. 3)
1. No *NN P* waves	−0.0441	
2. *NN P* waves in gnd. state only	−0.0434	
3. *NN P* waves in gnd. state & continuum	−0.0839	
4. (---)+$^1P_1$ in int. rescatt. state	−0.0900	−0.0061
5. (---)+$^3P_0$ in int. rescatt. state	−0.0711	0.0128
6. (---)+$^3P_1$ in int. rescatt. state	−0.0575	0.0264
7. (---)+$^3P_2$ in int. rescatt. state	−0.0790	0.0049
8. (---)+$^1P_1$,$^3P_0$,$^3P_1$,$^3P_2$ in int. rescatt. st.	−0.0454	0.0385

TABLE IV. Results of Faddeev calculations for $^1H(\vec{d},\gamma)^3He$, at $E_{d_{lab}}=29$ MeV, done to identify the dominant NN P-wave piece.

Calculation	T_{20} ($\theta_{lab}=90°$)	Δ (rel. to calc. No. 3)
1. No NN P waves	−0.0354	
2. NN P waves in gnd. state only	−0.0348	
3. NN P waves in gnd. state & continuum	−0.1004	
4. (---)+$^1P_1$ in int. rescatt. state	−0.1047	−0.0043
5. (---)+$^3P_0$ in int. rescatt. state	−0.0909	0.0095
6. (---)+$^3P_1$ in int. rescatt. state	−0.0684	0.0320
7. (---)+$^3P_2$ in int. rescatt. state	−0.0938	0.0066
8. (---)+$^1P_1$,$^3P_0$,$^3P_1$,$^3P_2$ in int. rescatt. st.	−0.0577	0.0427

ing a given set of intermediate P-wave states. The Δ value listed represents the change in T_{20} relative to the third calculation.

The result of this theoretical analysis shows that at all three energies examined, the NN P waves in the ground state play no role in determining $T_{20}(90°)$. The role of the NN P waves in the continuum state seem to vary with energy. At $E_d(\text{lab})=8$ MeV, the continuum NN P waves play only a very small role. The primary NN P-wave strength at this energy comes from the intermediate rescattering state. At $E_d(\text{lab})=19.8$ MeV, the NN P waves in the continuum change $T_{20}(90°)$ significantly. However, it turns out that at this energy, the NN P waves in the intermediate rescattering state pull $T_{20}(90°)$ in the other direction, and the net result is that the total NN P-wave strength at this energy is cancelled out [see also Fig. 4 at $E_d(\text{lab})=19.8$ MeV]. At $E_d(\text{lab})=29.2$ MeV, the NN P waves in the intermediate rescattering state are still pulling $T_{20}(90°)$ in the opposite direction as the NN P waves in the continuum state, but this time the NN P waves in the rescattering state are stronger, and thus there is a noticeable net NN P-wave strength at this energy. By examining the values of Δ for the calculations done at each energy, one clear conclusion can be drawn: the $^3P_1$ is the dominant NN P-wave component in determining the $^1H(\vec{d},\gamma)^3He$ $T_{20}(90°)$ observable. After the $^3P_1$, the $^3P_0$ is next in importance.

The dominance of the $^3P_1$ component in the current calculations can be justified by the following observations. Firstly, the $^1P_1$ component would not be expected to dominate because it is associated with a singlet spin state which cannot couple to the ^3He D state ($L=2$, $S=3/2$) via the $E1$ operator (because all of the spins in the D state are aligned). Of the remaining P-wave components, we can make an estimate as to which will dominate based on the value of the angular momentum (l) between the continuum P-wave NN pair (in the rescattering state) and the third spectator nucleon. Only for the $^3P_1$ component are there $l=0$ contributions for both the $J=1/2$ and $J=3/2$ states of the continuum (where J is the total angular momentum). Therefore, at the low energies where s-wave scattering is strong [$E_d(\text{lab})\leqslant 30$ MeV], it is expected that the $^3P_1$ component would be the strongest contributor, which is what the detailed calculations bear out. This result is interesting to compare with the results from polarized N-D elastic scattering, where it has also been found that the observables are sensitive to the NN P-wave interaction. Examples of this P-wave sensitivity can be found in the comparison of Faddeev calculations to T_{20} measurements of polarized p-D elastic scattering [5] and to A_y measurements of polarized n-D elastic scattering [6]. In the n-D case, for the A_y observable, a series of Faddeev calculations using the Bonn potential were used to identify the $^3P_0$ component as the most important NN P-wave piece. It should be emphasized that the above arguments for the dominance of the $^3P_1$ component in $^1H(\vec{d},\gamma)^3He$ should not be expected to hold for N-D elastic scattering due to the different selection rules which are present (i.e., electromagnetic vs strong force operator). The electromagnetic operator at these energies is especially sensitive to continuum dynamics due to the fact that only a limited number of multipolarities come into play (the $E1$ component dominates). Because of this, the role of particular continuum partial waves is perhaps more easily studied.

In summary, the present results provide a measurement of the energy dependence of $T_{20}(\theta_{lab}=90°)$ in a previously unexplored region. The new exact three-body calculations that we have done predict that the $T_{20}(\theta_{lab}=90°)$ observable should be strongly sensitive to the NN P-wave interaction in this energy region, and this prediction is supported by the data. Furthermore, we have identified the $^3P_1$ component as the dominant NN P-wave piece in determining the $T_{20}(\theta_{lab}=90°)$ observable in this energy regime. This result contrasts with the conclusions from polarized N-D elastic scattering measurements where it is found that the $^3P_0$ NN partial wave contribution is the dominant piece.

The authors would like to thank M. A. Godwin, C. M. Laymon, and J. C. Riley for help in data acquisition. The authors would also like to acknowledge the work of L. H. Kramer in designing the recoil-detection chamber that was used. This work was supported in part by the U. S. DOE Grant. No. DEFG05-91-ER40619. The work of A. C. F. was supported in part by JNICT Grant No. 1004/93, and the work of D. R. L. was partially supported by U. S. DOE Grants No. DE-FG05-86-ER40270 and No. DE-FG02-95ER40907.

[1] A. C. Fonseca and D. R. Lehman, Phys. Rev. C **48**, R503 (1993).
[2] M. Lacombe *et al.*, Phys. Rev. C **21**, 861 (1980).
[3] A. C. Fonesca and D. R. Lehman, Phys. Lett. B **267**, 159 (1991).
[4] A. C. Fonesca and D. R. Lehman, Few Body Syst. Suppl. **6**, 279 (1992).
[5] H. Witala, W. Glöckle, and Th. Cornelius, Nucl. Phys. **A496**, 446 (1989).
[6] W. Tornow *et al.*, Phys. Lett. B **257**, 273 (1991).
[7] T. B. Clegg, Rev. Sci. Instrum. **61**, 385 (1990).
[8] L. H. Kramer, Ph.D. thesis, Duke University, 1992.
[9] H. H. Barschall and W. Haeberli, *Polarization Phenomenon in Nuclear Reactions* (University of Wisconsin Press, Madison, 1971).
[10] K. Stephenson and W. Haeberli, Nucl. Instrum. Methods **169**, 483 (1980).
[11] M. C. Vetterli *et al.*, Phys. Rev. Lett. **54**, 1129 (1985).
[12] F. Goeckner, W. K. Pitts, and L. D. Knutson, Phys. Rev. C **45**, R2536 (1992).
[13] R. Machleidt, Adv. Nucl. Phys. **19**, 189 (1989).
[14] A. C. Fonesca and D. R. Lehman, in *Contributed Papers Book for the 14th International IUPAP Conference on Few-Body Problems in Physics*, edited by Franz Gross (College of William and Mary, Williamsburg, VA, 1994), p. 50; *Few Body Problems in Physics*, edited by Franz Gross, AIP Conf. Proc. 334 (AIP, New York, 1995), p. 478.
[15] J. Haidenbauer and W. Plessas, Phys. Rev. C **30**, 1822 (1984); **32**, 1424 (1985); J. Haidenbauer, Y. Koike, and W. Plessas, *ibid.* **33**, 439 (1986); W. Plessas, Lect. Notes Phys. **273**, 137 (1987); W. C. Parke, Y. Koike, D. R. Lehman, and L. C. Maximon, Few-Body Systems **11**, 89 (1991).
[16] K. Sagara *et al.*, Phys. Rev. C **50**, 576 (1994).
[17] J. Jourdan *et al.*, Nucl. Phys. **A453**, 220 (1986).